Investigation of the Frozen Bath Layer under Cold Anodes

Donald Picard[1], Jayson Tessier[2], Guillaume Gauvin[3], Donald Ziegler[4], Houshang Alamdari[5] and Mario Fafard[6]

1. Research Engineer
3. Research Engineer
5. Professor
6. Professor

NSERC/Alcoa Industrial Research Chair MACE[3] and Aluminium Research Centre – REGAL, Université Laval, Québec, Canada

2. Manager, Pilot Zone Operations

Alcoa Primary Metals Smelting Center of Excellence, Deschambault, Québec, Canada

4. Program Manager – Modeling

Alcoa Primary Metals, Alcoa Technical Center – Alcoa Center, PA, USA

Corresponding author: Donald.Picard@gci.ulaval.ca

Abstract

Hall-Héroult cell stability is highly affected by anode changing operation. Insertion of a cold anode in a cell will freeze a thick layer of molten cryolite under it. Its thickness, microstructure, and chemical composition vary as a function of time and location in the cell. To better understand the evolution of the frozen layer, mandatory for the validation of numerical models, a measurement campaign was conducted on the anodes having a few hours of operation in the cell. The macrostructure of the selected frozen bath samples has been highlighted using computed tomography while Scanning Electron Microscope (SEM) has been used to qualify its microstructure. An Energy-Dispersive X-Ray Spectroscope (EDS) coupled to the SEM has allowed the qualification of the chemical content. The investigation showed very different macrostructures between samples but also within them. Nevertheless, for all samples, there is a clear distinction between the frozen cryolite and alumina/dusting phases, the latter ones surrounding the cryolite matrix.

Keywords: Cryolite; anode; Computed Tomography; microstructure; anode changing.

1. Introduction

Large scale aluminium production is based on the Hall-Héroult electrolysis process, in which alumina is dissolved in molten cryolitic bath ($Na_3AlF_6 + (AlF_3)_{excess} + CaF_2 + Al_2O_3$) [1]. The electrolysis of dissolved alumina (Al_2O_3), performed using an electrolysis cell [2] (4 - 5 V and typically 200 - 400 kA), is occurring at approximately 960 °C and leads to the carbon consumption of the anode through the global reaction defined in Equation (1). Hence, this electrode needs to be replaced after 25 - 27 days of operation through an anode changing operation. However, the lifespan of the anode may vary by a few days depending of cell technology.

$$2Al_2O_{3\,(\text{dissolved in cryolite})} + 3C_{(anode)} \xrightarrow{12\,e^-} 4Al_{(liquid)} + 3CO_{2\,(\text{gas})} \quad (1)$$

Insertion of a new and cold anode at potroom temperature (~ 25 - 40 °C) in a molten cryolite bath at 960 °C will disturb the stability of the cell in many ways simultaneously [3-5]. From a thermal point of view, upon the insertion the cold anode, few centimeters of cryolitic bath will freeze under it and will melt within the next few hours of operation. Hence, thermal balance will

be affected during this period. In addition, density variation due to cryolite phase change (solidification/fusion) will lead to bath volume changes [6, 7]. Some researchers are now using numerical tools to simulate the anode change to estimate its impact on heat transfer in the electrolysis cell [3 - 5, 8].

The simulation of cryolite phase change underneath and around the anode requires characterization of both liquid and solid bath to be able to validate those models. Recently, Poncsák et al. [9] have studied the impact of the heat flux on the solidification of on unstirred cryolitic bath. They have highlighted the fact that high solidification rate can block diffusion of ions [1, 6, 7] and preserve chemical composition of cryolite. On the other hand, a slower solidification rate will alter bath composition and consequently all its properties. Poncsák et al. [9] also studied two different scenarios of cryolitic bath solidification without electrolysis in a laboratory scale experiment: A transient one where the temperature evolution of the cold anode surface (represented by a cold finger steel probe) is dictated by the bath temperature and a near steady-state one where the finger steel probe surface is stabilized at around 775 °C. The latter case may be more representative of the industrial case considering the large thermal inertia of carbon anodes. The two cases study led to two very different frozen cryolite structures. First, the transient case led to two morphologically distinct solidified bath layers. The first layer, in direct contact with the probe and thus with a high cooling rate, is dense with a relatively homogeneous morphology. The cooling rate of the second layer was lower and led instead to a brittle porous structure. In the second case, i.e. the near steady-state one, similar observations have been made but with lesser morphological variations between the high and low cooling rate zone. The structure and composition of the frozen cryolitic bath are hence highly correlated with the heat transfer occurring near cold surfaces [9 - 11].

As pointed out previously, chemical composition and morphology of frozen cryolitic bath are highly heat flux dependent. Both can affect the frozen cryolite density thus the volume change estimation, which is a very useful parameter in numerical model calibration [8]. However, based on plant observations, at least another phenomenon must be taken into account in the frozen bath apparent density evaluation: gas trapped in the frozen cryolite. Thus, the objective of this work is to analyze morphology of frozen bath sample taken from industrial anode after few hours of operation to get insights of the influence of operational conditions on frozen bath chemical composition and apparent density. The origin of the gas trapped is still under investigation and will not be discussed here.

2. Material and Method

Solidified bath samples were taken from anodes after only few hours of operation at Alcoa Deschambault smelting plant, Quebec, Canada (ADQ) . Frozen bath morphology highly depends of the anodes history, such as anode initial temperature, position in the cell, surface integrity, cell stability, etc. All those parameters can affect the heat flux and bath composition near the newly inserted anodes. Also, the dusting events in the cell can also influence the samples' morphology. Knowing all this, two very different samples from different anodes and operating time of those anodes, have been chosen and are presented in Figure 1. Sample A was chosen based on the fact that its structure seems to be relatively homogeneous with a minimum of porosity (from outside observation). On the other hand, Sample B was selected based on its very porous structure and its near constant thickness. In both cases, the sample surface in contact with the anode has been damaged while removing the sample.

Macroscopic morphological analysis has been performed using a X-ray tomograph, (Siemens Somatom Sensation 64) located at the INRS-ETE in Quebec city. This tomograph has been used in previous studies on carbon anode characterization and all details can be found in [12, 13]. In summary, X-ray computed tomography (CT) allows 3D density analysis without damaging the

sample structure. The output of the CT scanner is a 3D volume reconstructed with images made of voxels. In the present study, the voxel size is 0.1453 x 0.1543 x 0.4 mm^3. The unit of voxel is the Hounsfield Unit (HU), which is linearly related to the X-ray absorption coefficient. In the Hounsfield scale, air (STP conditions) has a value of -1000 HU and distilled water (STP conditions) has a value of 0. In term of grayscale image, the brighter the voxel, the denser the material. The information can then be used to evaluate the density ($kg \cdot m^{-3}$). Depending of the voxel resolution and sample microstructure scale, the density obtained will be either the real or apparent one. In the present case the voxel unit is kept in Hounsfield scale (HU) and will be related to the apparent density.

For microstructure analysis, a scanning electron microscope SEM JEOL JSM-840A has been used to obtain surface topology of the samples. The chemical analyses have been done with an NORAN energy dispersive spectrometer coupled to the SEM.

Sample A **Sample B**

Figure 1. Photos of the frozen bath samples A and B. The bottom of each sample was in contact with their corresponding anode.

3. Results and Discussion

3.1. Computed Tomography

3.1.1. Sample A

CT volume reconstruction of Sample A is shown in Figure 2. The average X-ray absorption coefficient of the whole sample is around 1650 HU. Two orthogonal images along sample length are shown in Figure 3 and are representative of the internal morphology of Sample A. Their locations are represented by the yellow line and red line in Figure 2. As expected from the external observation, internal structure of Sample A is relatively homogeneous (Figure 3). It is however clear that it contains very large pores. These large pores (larger than the voxel resolution) account for 3 % in Figure 3a and for 3.5 % in Figure 3b of the sample volume. Hence, in that case, neglecting them may not have an important impact on the total frozen bath volume estimation through numerical investigation without considering the presence of gas.

Also, contrary to the observation made by Poncsák et al. [9] in laboratory experiments, no layer is apparent in Figure 3. Spatial location of the frozen sample seems however to have an influence on density distribution as highlighted on Figure 3a and Figure 3b. Neglecting the large porosities, frozen bath of Figure 3a tends to have a more homogeneous density distribution than the one in Figure 3b. Based on the laboratory observations of Poncsák et al. [9] in the near steady-state case, it may be assumed that frozen bath shown in Figure 3a has seen a fast cooling rate leading to this more homogeneous density distribution. However, density distribution shown in Figure 3b, led to different observations. At this location (red line in Figure 2) the central part of Sample A is less dense than the outer region. This unconventional internal

structure indicates freezing directionality in the central part that may be related to a change in the freezing direction related to an uncommon event in the cell. To highlight this, Figure 4 shows the X-ray absorption coefficients distribution and its histogram along the blue line shown in Figure 3b. The histogram reveals clearly the two distinct zones. The middle part of the sample has an average of 1600 HU and this value increase to 1950 for outer region, which correspond to an increase of approximately 11 % in term of density. Those values do not take into account the large porosities, which ones can be seen at the far left of the histogram. As the denser region of the thicker part of Sample A is located around the sample, the density variations cannot be only related the cooling rate as observed by Poncsák et al. [9] in a controlled environment.

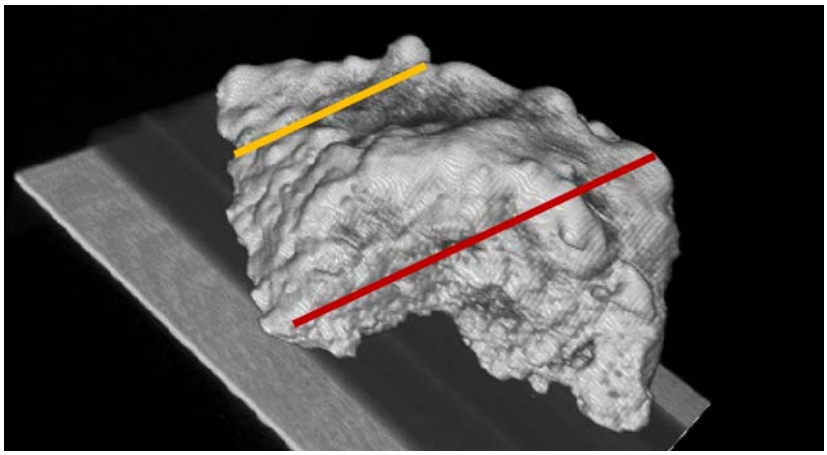

Figure 2. Volume reconstruction of sample A based on X-ray tomography.

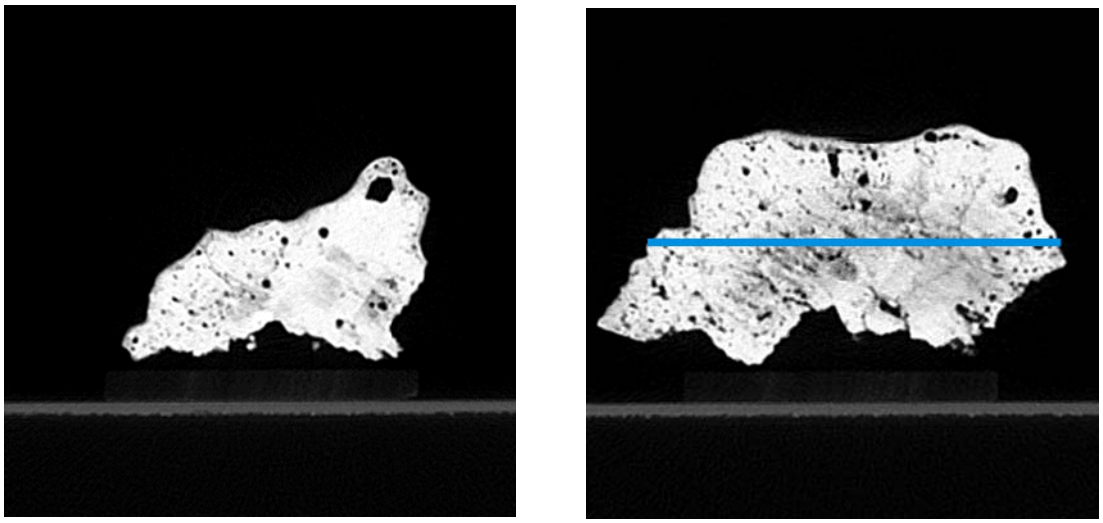

a) **b)**

Figure 3. X-ray images of sample A. a) Location represented by the yellow line in Figure 2 b) Location represented by the red line in Figure 2.

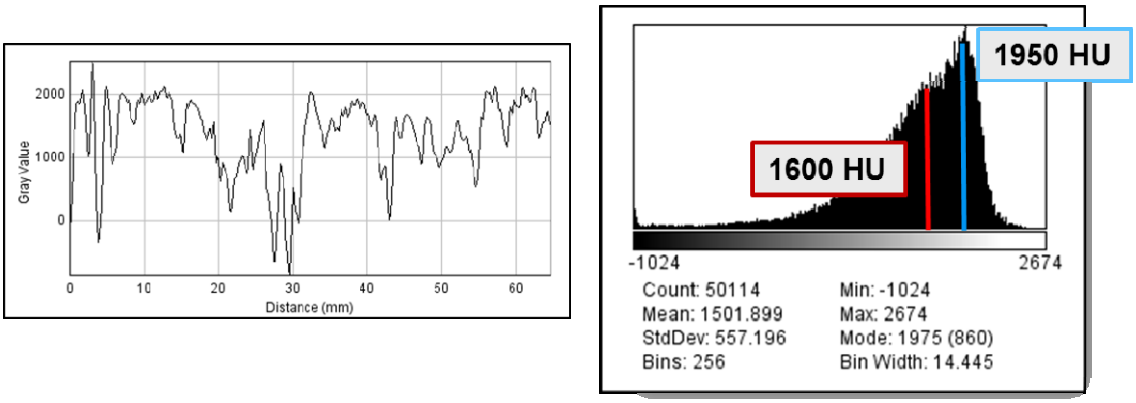

Figure 4. X-ray absorption coefficients (HU) distribution (left) and histogram (right) at the middle height of Figure 3B (blue line).

3.1.2. Sample B

CT volume reconstruction of Sample B is shown in Figure 5. The average X-ray absorption coefficient of the whole sample is 1211 HU. Two orthogonal images along sample length are shown in Figure 6 and are representative of the internal morphology of Sample B. Their locations are represented by the yellow line and red line in Figure 5.As expected from the external observation, internal structure of Sample B is very porous (Figure 6). It is also very clear that it contains very large pores. These large pores (larger than the voxel resolution) account for 10 % in Figure 6a and close to 16 % in Figure 6b. Hence, in that case, neglecting this porosity level will have an important impact on the total frozen bath volume estimation in numerical simulation without considering gases. The frozen bath morphology already indicates that it comes from an anode having a completely different history that the one associated with Sample A.

Also, contrary to the observation made on Sample A, Sample B seems to have two distinct layers as shown in Figure 6. As observed experimentally by Poncsák et al. [9], the bottom layer which has been very close to the cold anode surface is more homogeneous than the outer layer. The latter was very brittle, very porous and also contained most of the large pores. Spatial location of the frozen sample also seems to have an influence on density distribution as highlighted on Figure 6 but to a lesser extent. Also, neglecting the large pores, frozen bath in the outer layer (the more porous one) in both Figure 6a and Figure 6b tends to have a homogeneous density distribution. This is highlighted in Figure 7 by showing the X-ray absorption coefficients distribution and its histogram along the blue line shown in Figure 6a. The average X-ray absorption coefficient in this zone is approximately 1500 HU. This value is very close to the one obtained in the lower density region of Figure 3 (central part of Sample A) indicating that both zones may be have similar chemical composition. Again, this value does not take into account the large porosities, which ones can be seen at the far left of the histogram. Even though Sample B seems to fit better the observation of Poncsák et al. [9], relating the morphology to the cooling rate, a chemical analysis is required to get some insight on the composition of each layer.

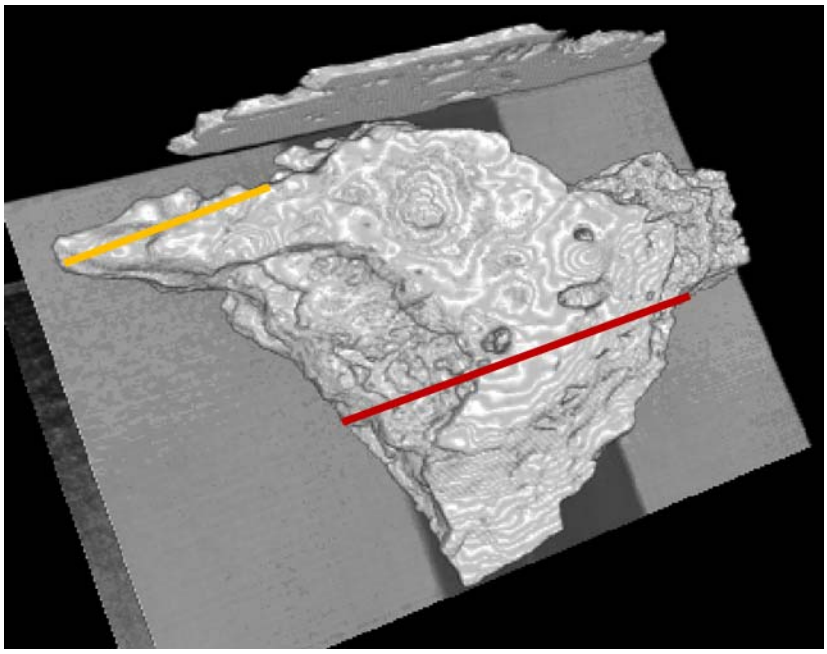

Figure 5. Volume reconstruction of sample B based on X-ray tomography.

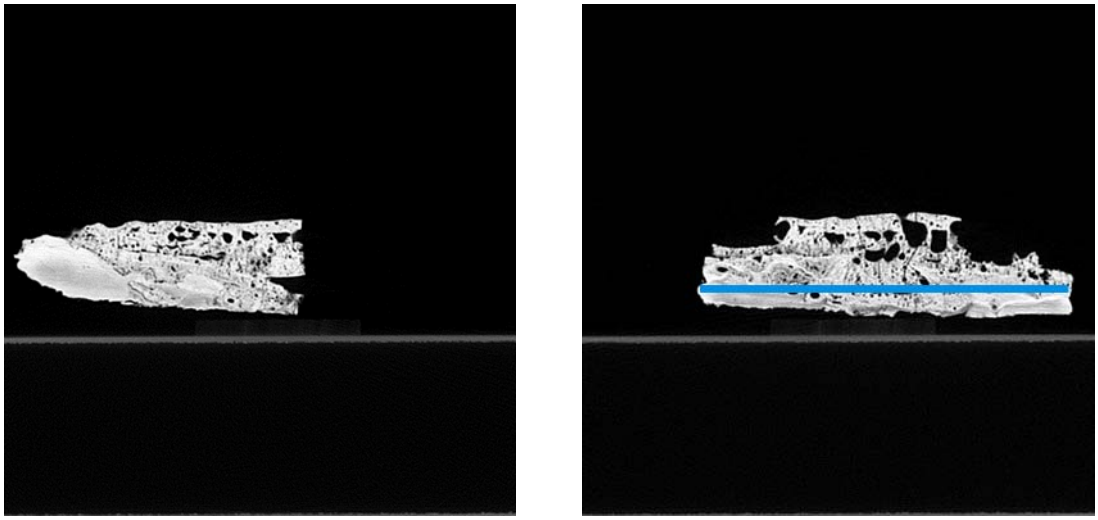

a) **b)**

Figure 6. X-ray images of sample B. a) Location represented by the yellow line in Figure 5. b) Location represented by the red line in Figure 5.

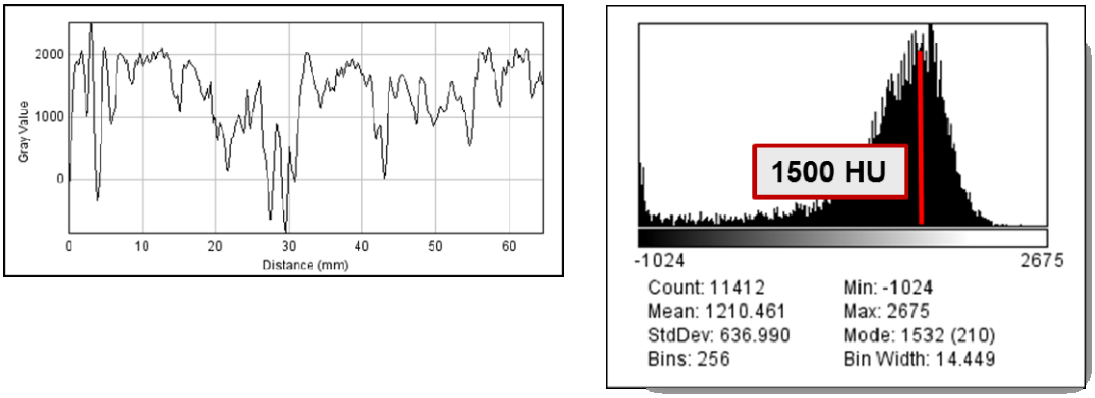

Figure 7. X-ray absorption coefficients (HU) distribution (left) and histogram (right) at the middle height of Figure 6B (blue line).

3.2. SEM/EDS

Sample A and B both contain regions with different morphologies. The CT data was however not sufficient to identify the nature of these regions as they could not be directly related to cooling rate [9]. Chemical qualitative analyses were then performed on both samples using a SEM JEOL JSM-840A (15 kV) coupled with an EDS NORAN.

The two regions of interest were the homogeneous region of Sample B (bottom layer shown in Figure 6b) and the high-density region (outer part of Sample A). Representative SEM images of the two regions of interest are shown in Figure 8. The high-density region (Figure 8a) seems to contain two types of structure: a large flaky zone and a small smooth and homogeneous one. On the other hand, the homogeneous region seems to contain more of the smooth structure and less of the flaky one. EDS has then been used to identify those two distinguished zones and typical results are shown in Figure 9. The smooth structure (Figure 9a) contains mainly sodium (Na), fluorine (F) and aluminium (Al). This structure is thus most probably frozen cryolite (Na_3AlF_6). Oxygen (O) and calcium (Ca) were also detected and may be related to alumina (Al_2O_3) in which Ca is a common impurity and is accumulating in the bath. The gold (Au) and palladium (Pd) are related to surface preparation. On the other hand, the flaky zone mainly contains Al and O, which is probably related to alumina (Al_2O_3). This zone also seems to contain some cryolite (F and Na) as well as some calcium impurities related to the alumina. Also, carbon (C) was found in both the smooth and the flaky structures. It may be assumed that the carbon found is related to anode dusting and also maybe to carbides. In the latter case, EDS could not be used to reveal the form of carbide. Also, as seen on the picture of Sample B (Figure 1) dusting (dark zone) seems to be indeed embedded within the sample. An SEM/EDS analysis of this region is shown in Figure 10. In that case, results show the presence of iron (Fe) and nickel (Ni) (most probably coming from the anode [14]) in addition to alumina and cryolite. Based on those analyses, the bottom layer of Sample B (which was in contact with the anode) is mostly cryolite frozen at high cooling rate, as observed by [9] in laboratory. However, the presence of gas, alumina (with its impurities) and dusting have affected the morphology of the upper layer of Sample B and the whole volume of Sample A. Hence, the results differ unsurprisingly from the laboratory observations.

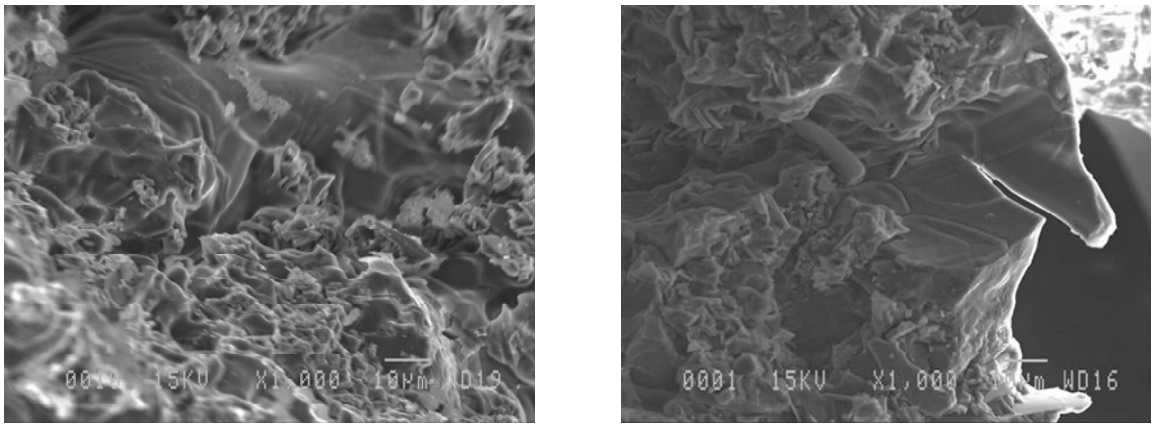

a) b)

Figure 8. SEM representative images of investigated zone. a) high density region. b) homogeneous zone.

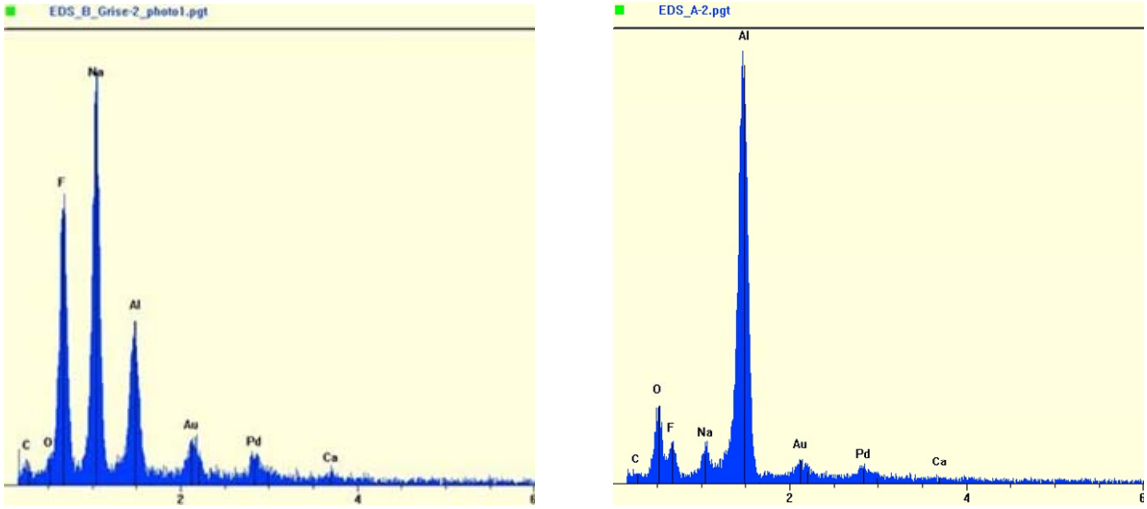

a) b)

Figure 9. Typical results of EDS analysis. a) Smooth and homogeneous zones. b) Flaky zones.

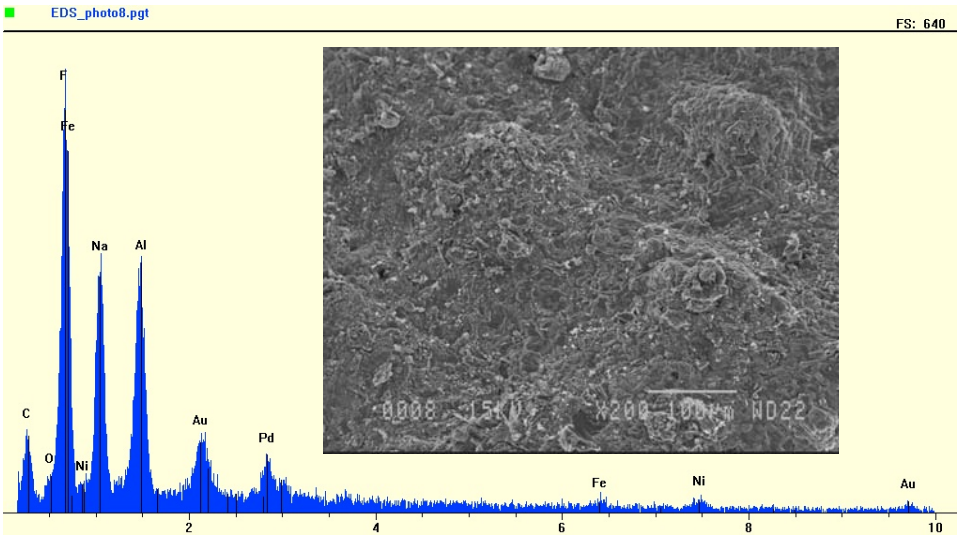

Figure 10. Typical results of SEM/EDS analysis of the dusting region of Figure 1 (Sample B).

4. Conclusion

Two bath samples that froze under newly inserted anode have been investigated with computed tomography and SEM/EDS method to highlight the difference with laboratory observations. The two samples were mainly chosen based on their very different morphologies. In both cases, the computed tomography reveals the large amount of big pores. The origin of those large pores is still under investigation. It may be assumed that they are related to unidentified gas movement mechanisms (e.g. expelling of dissolved gas from the bath during the freezing process). Except for those large pores, morphology of Sample B seems to suit the experimental observations of Poncsák et al. [9] regarding the effect of the cooling rate on the frozen cryolitic bath morphology. However, the Sample A morphology differs largely from laboratory observations and highlights the difference between laboratory and *in situ* experiments. This was mainly shown on the SEM/EDS analyses where undissolved alumina and carbon dust were found in samples. Finally, all these observations reveal the importance of taking into account the presence of gases, which led to the formation of large pores in the frozen bath samples and thus may affect the volume estimation of the frozen ledge underneath the anodes.

5. Acknowledgments

Authors would like to acknowledge the financial support of Natural Sciences and Engineering Research Council (NSERC) and Alcoa. A part of the research presented in this paper was financed by the Fonds de Recherche du Québec-Nature et Technologie (FRQ-NT) by the intermediary of the Aluminium Research Centre-REGAL. Particular thankfulness is dedicated to Clement Andriamirado, from INSA Rouen, for his help for data analysis.

6. References

1. Jomar Thonstad, Aluminum electrolysis, electrolyte and electrochemistry. 1987, Amsterdam: Elsevier.
2. Morten Sørlie and Harald A. Øye, Cathodes in Aluminium Electrolysis. 3rd edition ed. 2010, Düsseldorf, Germany: Aluminium-Verlag Marketing & Kommunikation GmbH.
3. V. Gusberti et al., Modeling the effect of the anode change sequence with a non-linear shallow water stability model, *Light Metals* 2007, 317-22.
4. Wang Qiang, Li Baokuan and Mario Fafard, Effect of Anode Change on Heat Transfer and Magneto-hydrodynamic Flow in Aluminum Reduction Cell, JOM. Vol. 68**,** No. 2, (2016), p. 610-22.
5. Qiang Wang et al., Numerical investigation on the impact of anode change on heat transfer and fluid flow in aluminum smelting cells, *Light Metals* 2016, 321-325.
6. Patrice Chartrand and Arthur D. Pelton, A predictive thermodynamic model for the Al-NaF-AlF3-CaF2-Al2O3 system, *Light Metals* 2002, 245-252.
7. Asbjorn Solheim and Lisbet I. R. Stoen, On the composition of solid deposits frozen out from cryolitic melts, *Light Metals* 1997, 325-332.
8. Min Li et al., Ledge Formation under the Consideration of its Interaction with Bath Composition and the Fluid Dynamic Motion, in *Encyclopédie de la recherche sur l'aluminium au Québec*, C.d.r.s.l.a.-. REGAL, Editor. 2015, Université Laval: Québec, Canada.
9. Sandor Poncsak et al., Impact of the heat flux on solidification of cryolite based bath, *Light Metals* 2016, 359-364.
10. Sandor Poncsak et al., Study of the structure and thermophysical properties of the side ledge in Hall-Heroult cells operating with modified bath composition, *Light Metals* 2015, 655-659.
11. Sandor Poncsak et al., Structural characterisation and thermophysical properties of the side ledge in hall-heroult cells, *Light Metals* 2014, 585-589.

12. Donald Picard et al., Characterization of prebaked carbon anode samples using X-ray computed tomography and porosity estimation, *Light Metals* 2012, 1283-1288.
13. Donald Picard et al., Characterization of a full-scale prebaked carbon anode using X-ray computerized tomography, *Light Metals* 2011, 973-978.
14. François Chevarin et al., Air and CO2 reactivity of carbon anode and its constituents: An attempt to understand dusting phenomenon, *Light Metals* 2015, 1147-1152.